Journal of Alloys and Compounds 509 (2011) 4073–4080

Contents lists available at ScienceDirect

Journal of Alloys and Compounds

journal homepage: www.elsevier.com/locate/jallcom

On the influence of small quantities of Bi and Sb on the evolution of microstructure during swaging and heat treatments in copper

F. Otto*, J. Frenzel, G. Eggeler

Ruhr-Universitaet Bochum, Institute for Materials, Universitaetsstr. 150, 44801 Bochum, Germany

ARTICLE INFO

Article history:
Received 23 September 2010
Received in revised form
22 December 2010
Accepted 24 December 2010
Available online 31 December 2010

Keywords:
Copper
Bismuth
Antimony
Rotary swaging
Microstructure
Thermomechanical processing

ABSTRACT

In the present work, the influence of small amounts of Bi and Sb on the microstructural evolution of Cu during an ingot metallurgy processing route is investigated. Both elements are known to segregate to grain boundaries in Cu. Cu ingots with an outer diameter of 40 mm containing 0.008 wt.% Bi and 0.92 wt.% Sb, respectively, were vacuum induction melted, cast, and gradually swaged down to a final diameter of 11.7 mm with several intermediate annealing steps. Subsequent annealing treatments were conducted to investigate the microstructural evolution of the swaged bars. Optical microscopy, hardness testing and orientation imaging microscopy were used to characterize the deformation and recrystallization behavior, as well as the evolution of texture in the alloys. The results are then compared to those obtained for pure Cu. It is shown that even small amounts of alloying elements significantly alter the hardening behavior and suppress recrystallization at low temperatures. At higher temperatures, recrystallization in Cu, Cu–Bi and Cu–Sb leads to different textures.

1. Introduction

The present work is part of a larger research program on the role of grain boundary chemistry and crystallography on creep cavitation in Cu-based alloys. In this research program, the formation of creep cavities is assessed for pure Cu and for Cu alloys with small quantities of Bi and Sb. Here, the focus lies on the processing of these three materials: Cu, Cu–Bi, and Cu–Sb. It is important to note that the solubility of Bi in Cu is very low (Fig. 1a) [1], reaching a maximum of 200 at.ppm at about 950 °C (Fig. 1b) [2]. In contrast, Cu can solve up to 10.6 wt.% Sb at 645 °C (Fig. 2). Both elements are known to cause embrittlement [3,4]. It has been known for a long time that this detrimental effect on mechanical properties is related to grain boundary segregation [5,6]. Early assumptions were experimentally verified by powerful analytical methods like Auger electron spectroscopy (AES) and analytical transmission electron microscopy (TEM) as they became available [7–11]. A number of dedicated studies have been conducted to understand atomistic, microscopic, and macroscopic aspects of Bi and Sb segregation to Cu grain boundaries [12–21]. In particular, the Cu–Bi system became a role model for performing studies ranging from the effect of grain boundary segregation on brittleness in polycrystalline material [22] to the detailed high resolution TEM investigation and atomistic modelling of specific segregation sites in tailor-made bi-crystals [23]. More recently, Bi and Sb were deliberately added to Cu in order to achieve certain properties. Thus, Bi is considered a suitable candidate for substituting toxic Pb in Cu-based alloys, which is added to improve machinability [24,25]. Furthermore, small quantities of both Bi and Sb are considered to be promising candidates to effectively stabilize nanocrystalline microstructures in Cu [26].

Therefore, the effect of small additions of Bi and Sb on the evolution of microstructure during processing is investigated. An ingot metallurgy processing route is considered, which involves melting, casting, solution annealing, and swaging with intermediate and subsequent heat treatments. The microstructural evolution in Cu alloys containing Bi and Sb is compared with the results of a recent study on pure Cu [27] in terms of grain size and texture. Processing parameters are identified that yield similar microstructures in all three materials.

2. Experimental methods and materials

Cylindrical oxygen-free high-conductivity (OFHC) Cu chunks (nominal purity greater than 99.99 wt.%) with a length of approximately 20 mm and an outer diameter of 13 mm were obtained from Norddeutsche Affinerie AG, Germany (now Aurubis AG). Cu master alloys containing 70 wt.% Bi and 60 wt.% Sb, respectively, were produced by Hauner Metallische Werkstoffe, Germany. The base materials for both master alloys had a nominal purity greater than 99.9 wt.%. These master alloys were taken together with pure Cu to produce the targeted alloy compositions of 0.008 wt.% Bi (Cu–Bi) and 0.92 wt.% Sb (Cu–Sb) by vacuum induction melting (VIM) in carbon crucibles under a pure Ar atmosphere of 600 mbar. This required feedstock compositions of 0.02 wt.% Bi (more than half of the Bi is lost) and 1 wt.% Sb (only some Sb loss).

* Corresponding author. Tel.: +49 (0)234 32 28982; fax: +49 (0)234 32 14235.
E-mail address: frederik.otto@rub.de (F. Otto).

0925-8388/$ – see front matter © 2010 Elsevier B.V. All rights reserved.
doi:10.1016/j.jallcom.2010.12.178

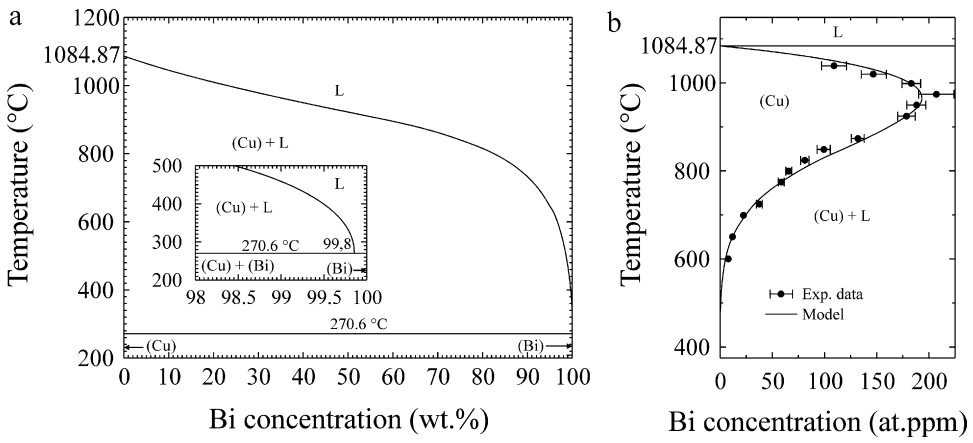

Fig. 1. (a) Cu–Bi phase diagram [1]. (b) Cu-rich side of the Cu–Bi phase diagram [2].

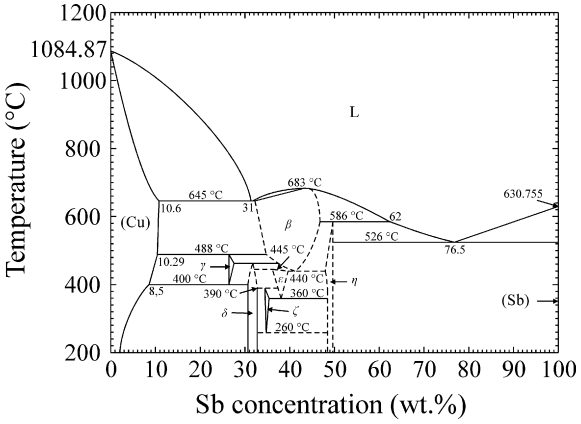

Fig. 2. Cu–Sb phase diagram [1].

The alloy melts were kept a few minutes above the liquidus temperature, and then cast into a preheated cylindrical steel mold coated with an yttria slurry. Details of the melting and casting procedure have been reported elsewhere [27]. The cast ingots were encapsulated into quartz tubes under a 500 mbar pure Ar atmosphere and solution annealed for 24 h at 950 °C followed by water quenching. Similar solution anneals have been shown to effectively remove segregation of Bi and Sb from grain boundaries after slow furnace cooling [28,29].

The chemical compositions of the ingots were determined after processing by Revierlabor GmbH, Germany. They are given in Table 1. The Bi contents at the top and at the bottom of the ingot were found to be equal indicating that Bi was homogeneously distributed throughout the ingot. The solution-annealed ingots were then subjected to a thermomechanical treatment consisting of several rotary swaging steps with intermediate annealing treatments. A detailed description of this type of thermomechanical treatment has been published elsewhere [27]. The ingots which had an initial outer diameter of 40 mm were swaged down to rods with a final outer diameter of 11.7 mm in nine steps. Four intermediate anneals with a duration of 900 s were conducted after swaging steps 2, 4, 6, and 7 (Table 2). A maximum temperature of 380 °C was applied during the four intermediate anneals [27]. After swaging, subsequent annealing was performed at two temperatures, 380 and 920 °C. Annealing times of 900 and 3600 s were applied. Temperature–time curves during heating to the two annealing temperatures 380 and 920 °C are published elsewhere [27]. The annealing temperatures were chosen to keep grain boundary segregation during thermomechanical processing at a minimum. At the low annealing temperature of 380 °C diffusion is too slow to establish strong grain boundary segregation [28], while at the high annealing temperature of 920 °C, more of the Bi and Sb go into solution due to higher bulk solubilities [1,2] and a decreased segregation tendency [11]. Furthermore, it has been demonstrated that such thermomechanical processing yields stable and homogeneous microstructures for pure Cu [27]. For studying phenomena related to equilibrium segregation at grain boundaries, additional annealing treatments at intermediate temperatures are required. This is, however, not a focus of the present study.

Radial and longitudinal cross-sections were cut from the cylindrical rods and mechanically polished down to a particle size of 1 μm. For optical microscopy, the specimens were color-etched for 75 s in Klemm's reagent no. 3 [30] and examined using a Leica DM4000 M optical microscope. Grain size profiles were measured at different positions on the longitudinal cross-sections using a linear intercept method. Seven reference lines of a length l_i ($i = 1 \ldots 7$) parallel to the longitudinal axis of the rods were used and the average grain size $d_{GS,i}$ was calculated as $d_{GS,i} = l_i/n_i$ where n_i is the number of intersected grains on line i. One reference line is located in the center axis of the rod corresponding to position 0 mm, two at a distance of 100 μm from the surfaces (positions ± 5.75 mm) and the remaining four in regular distance intervals in between (for a schematic illustration see [27]).

Orientation imaging microscopy (OIM) was performed in the scanning electron microscope (SEM) to study the evolution of microstructure and texture. Good surface qualities are required for these investigations and, therefore, additional vibratory polishing (Buehler Vibromet 2) was conducted using colloidal silica with a particle size of 0.06 μm. OIM was performed using an SEM of type Leo 1530 VP equipped with a field-emission gun and an EDAX-TSL EBSD system. An operating voltage of 28 kV was used for OIM. Typical working distances and scan step sizes for OIM were 20 mm and 1.5 μm, respectively. In order to study the local evolution of microstructure, scans were performed from the center to the outside of the radial cross-sections, as schematically depicted in Fig. 3.

Cross-bar hardness profiles were recorded on longitudinal cross-sections using a semi-automatic Vickers hardness tester of type KB30BVZ (KB Prüftechnik GmbH, Germany). A test load of 1.96 N was applied corresponding to HV0.2. Three hardness profiles were recorded and averaged for each specimen. The distance between individual hardness indents was 0.5 mm.

Table 1
Chemical composition of the Cu–Bi and Cu–Sb alloys after casting and solution annealing in wt.%. All elements not shown here were below the detection level.

	Cu–Bi (top)	Cu–Bi (bottom)	Cu–Sb
Bi	0.008	0.008	<0.002
Sb	<0.002	<0.002	0.92
C	0.003	–	0.003
O	0.0009	–	0.0036

Table 2
Processing parameters. The resulting degree of deformation, φ_i, is calculated according to $\varphi_i = 2 \times \ln(d_i/d_{i+1})$ where d_i and d_{i+1} are the outer diameters of the rods before and after each swaging step.

Processing sequence
39.4 mm > 37.3 mm, $\varphi = 0.11$
37.3 mm > 33.4 mm, $\varphi = 0.22$
900 s, 380 °C
33.4 mm > 29.5 mm, $\varphi = 0.25$
29.5 mm > 25.6 mm, $\varphi = 0.28$
900 s, 380 °C
25.6 mm > 22.1 mm, $\varphi = 0.29$
22.1 mm > 19.1 mm, $\varphi = 0.29$
900 s, 380 °C
19.1 mm > 16.1 mm, $\varphi = 0.34$
900 s, 380 °C
16.1 mm > 13.7 mm, $\varphi = 0.32$
13.7 mm > 11.7 mm, $\varphi = 0.32$
Annealing at 380 or 920 °C, respectively

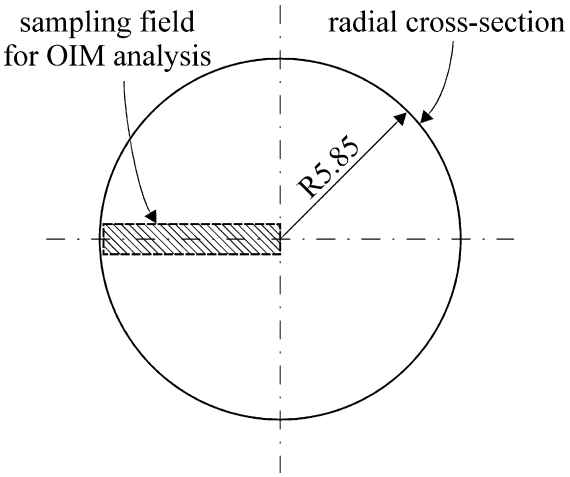

Fig. 3. Position of the sampling field for OIM analysis on radial cross-sections with an outer diameter of 11.7 mm.

3. Results

3.1. Optical macro- and micrographs and hardness results

Macrographs of cross-sections from Cu (investigated previously in Ref. [27]), Cu–Bi and Cu–Sb ingots in the as-cast (left column of Fig. 4) and cast and solution-annealed condition (right column of Fig. 4) are shown in Fig. 4a–c. The grain sizes in the as-cast and solution-annealed conditions appear to decrease with increasing amounts of alloying additions. A small region of equiaxed grains characterizes the centers of the cast and solution annealed Cu–Bi and Cu–Sb ingots (Fig. 4b and c). Evidence for dendritic microstructures were only observed in the as-cast Cu–Sb (not shown here), where the dendritic features disappear during solution annealing. As one would expect, solution annealing resulted in some grain coarsening in all three alloys.

The macrographs presented in Fig. 5 show the longitudinal and radial cross-sections of the Cu–Bi ingot after swaging. As described for the case of pure Cu [27], grains stretch out along the longitudinal axis of the rod (Fig. 5a). The spiral arrangement of grains in the outer parts of radial cross-sections is a striking feature of the as-swaged microstructure (Fig. 5b). This spiral arrangement gives some insight into the nature of plastic deformation during swaging, which is not considered further in the present study. The features outlined here do not differ from what was previously reported for pure Cu [27].

Annealing at 380 °C for 900 s does not trigger extensive recrystallization events. In the microstructures shown in Fig. 6a and b, strongly deformed regions can be recognized while new grains are absent. This is not in line with what has been reported for pure Cu, where these conditions led to full recrystallization [27]. Even increasing annealing times up to 3600 s (Fig. 6c and d) only results in partial recrystallization. The center of the rod is characterized by small recrystallized grains, while only very few new grains have formed in the outer regions (Fig. 6c and d). Full scale recrystallization is observed after 920 °C anneals after 900 and 3600 s (Fig. 7). Both annealing times yield fairly homogeneous, equiaxed grain

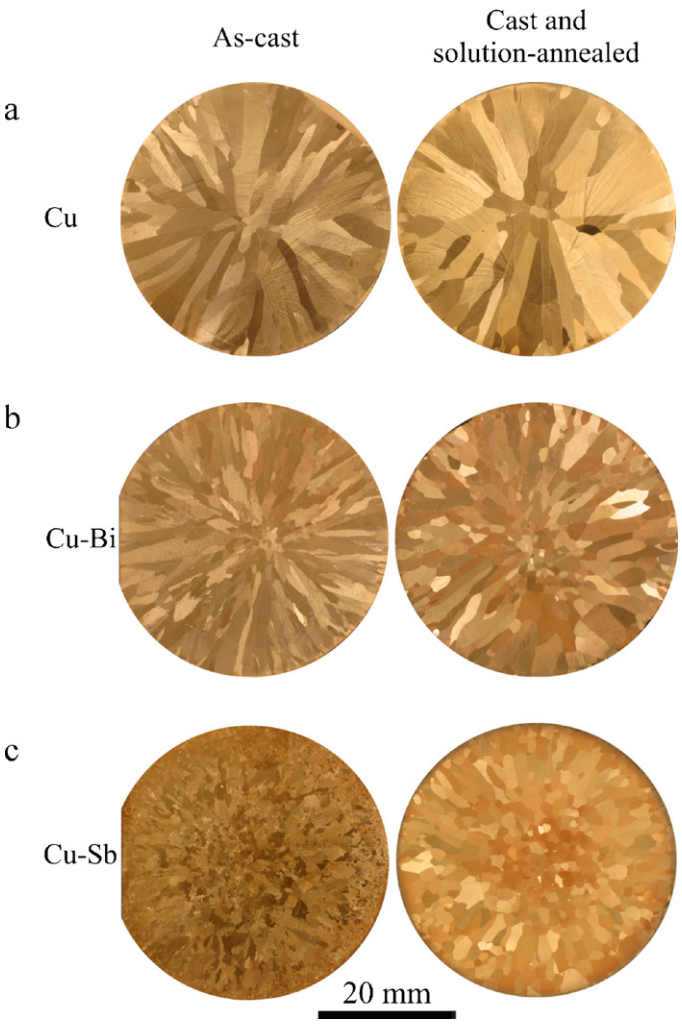

Fig. 4. Cross-sectional macrographs of as-cast and subsequently solution-annealed (950 °C, 24 h) cylindrical ingots of (a) Cu, (b) Cu–0.008 wt.% Bi, and (c) Cu–0.92 wt.% Sb.

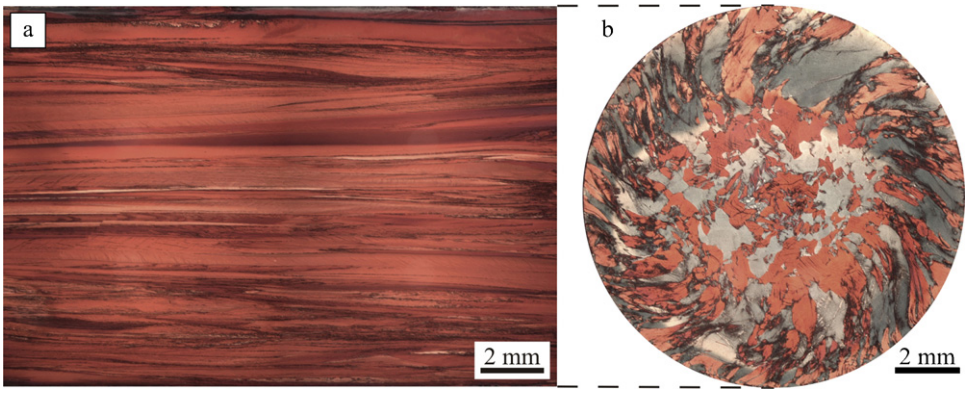

Fig. 5. Microstructures of the Cu–0.008 wt.% Bi alloy after swaging, without subsequent temperature exposure. (a) Radial cross-section and (b) longitudinal cross-section.

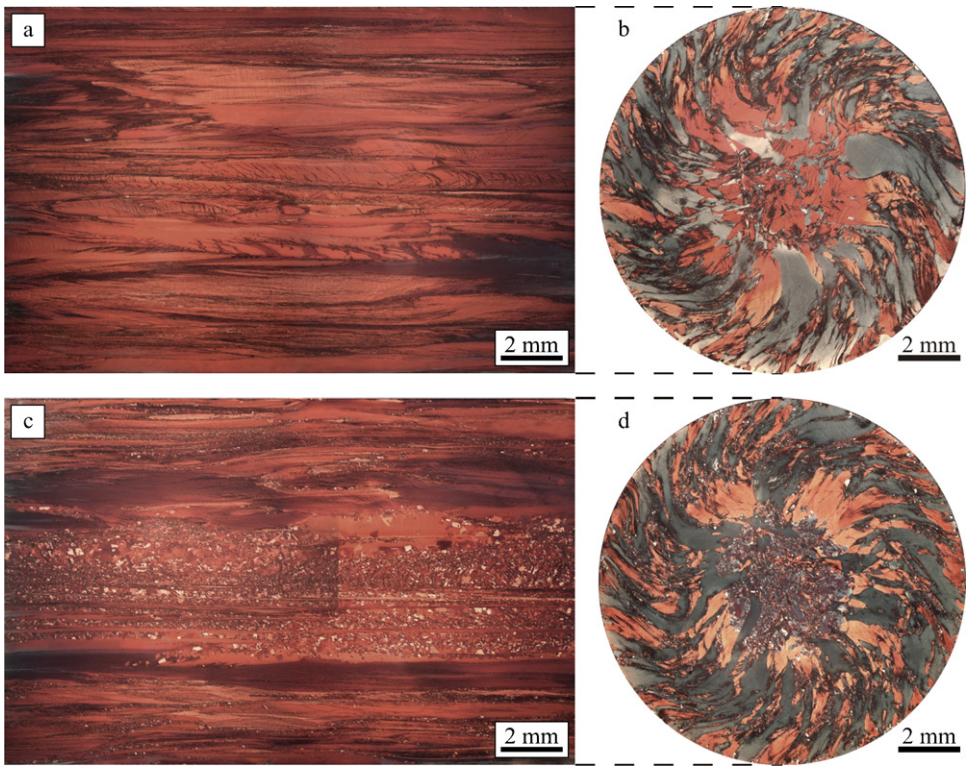

Fig. 6. Microstructures of Cu–0.008 wt.% Bi rod after swaging and subsequent annealing. (a) Longitudinal and (b) radial cross-section after heating to 380 °C in 900 s. (c) Longitudinal and (d) radial cross-section after extending the duration of the heat treatment to 3600 s.

structures. The microstructures of the Cu–Sb alloy (not shown here) look very similar.

Cross-bar grain size distributions of fully recrystallized Cu–Bi and Cu–Sb are given in Fig. 8a. Data for pure Cu subjected to an identical thermomechanical treatment are also included for comparison (Fig. 8b). Homogeneous grain size distributions are obtained after annealing up to 920 °C for all materials. Mean grain sizes in the center of the rods after 900 s annealing are approximately 400 and

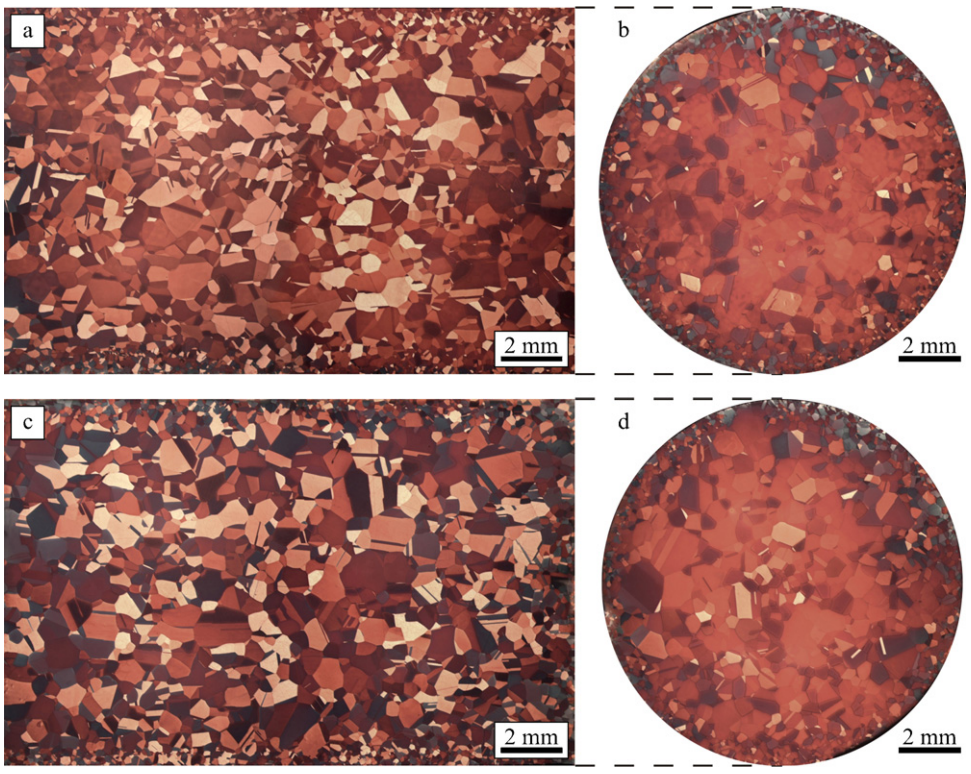

Fig. 7. Microstructures of Cu–0.008 wt.% Bi rod after swaging and subsequent annealing. (a) Longitudinal and (b) radial cross-section after heating to 920 °C in 900 s. (c) Longitudinal and (d) radial cross-section after extending the duration of the heat treatment to 3600 s.

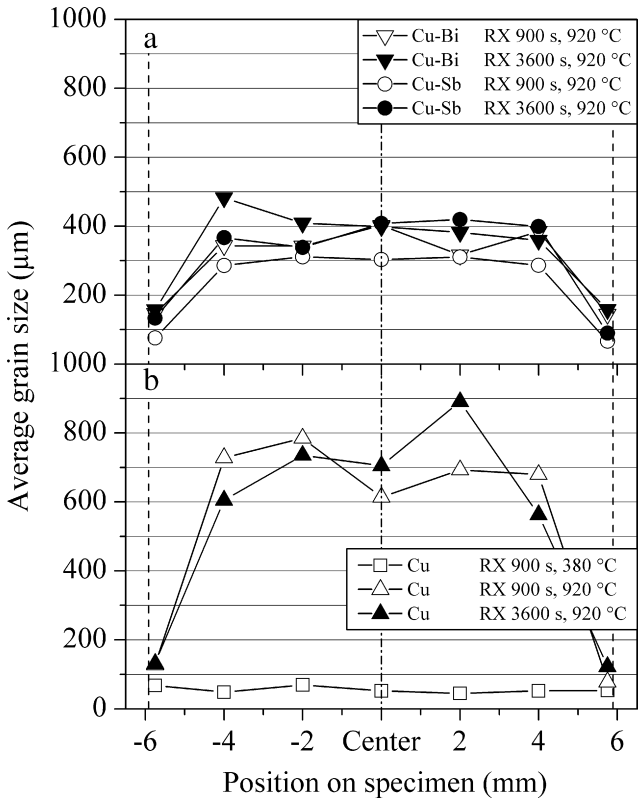

Fig. 8. Cross-bar grain size distributions for the fully recrystallized (a) Cu–Bi, and Cu–Sb and (b) for the Cu rods. The durations and temperatures given in the legend refer to the recrystallization heat treatment.

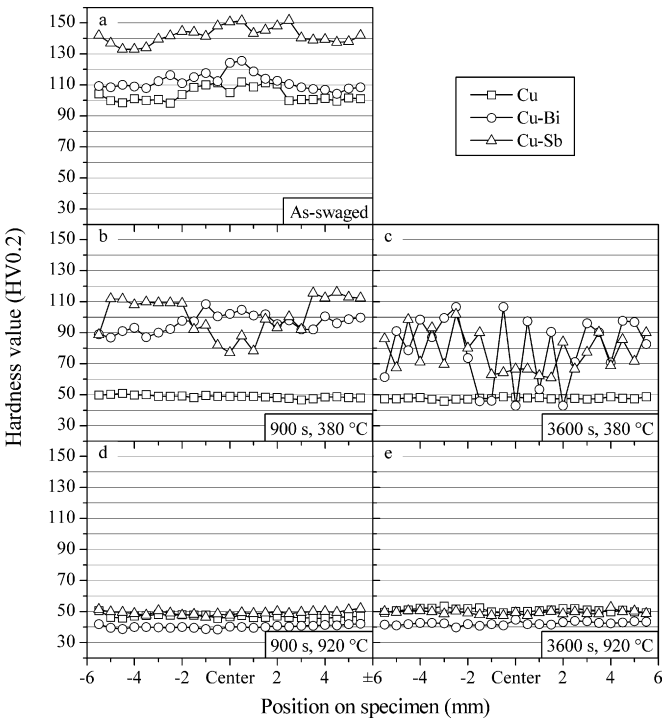

Fig. 9. Cross-bar hardness profiles for the (a) as-swaged material state and after subsequent annealing: (b) 900 s at 380 °C; (c) 3600 s at 380 °C; (d) 900 s at 920 °C; (e) 3600 s at 920 °C.

300 μm for Cu–Bi and Cu–Sb, respectively. Grain sizes of approximately 150 μm (Cu–Bi) or 70 μm (Cu–Sb) are measured in the thin cylindrical regions close to the surfaces of the rods. Increasing the annealing time to 3600 s only results in a slight increase in grain size. For pure Cu, the grain size after recrystallization at 920 °C is almost twice as high than in Cu–Bi and Cu–Sb. In contrast to Cu–Bi and Cu–Sb, pure Cu fully recrystallizes and establishes a homogeneous grain size of 50 μm at 380 °C (Fig. 8b).

Cross-bar hardness profiles are shown in Fig. 9. Directly after swaging, the highest hardness values of up to 150 HV0.2 are obtained for the Cu–Sb alloy. Pure Cu exhibits the lowest hardness values ranging from 100 to 110 HV0.2 (Fig. 9a). For all materials investigated here, the highest hardness values are found in the center of the rod in the as-swaged state. Subsequent annealing at a temperature of 380 °C leads to a significant decrease in hardness for all materials (Fig. 9b). While hardness values are constant over the cross-section of the pure Cu rod (close to 50 HV0.2), strong variations in local hardness characterize Cu–Bi and Cu–Sb. A heat treatment of 900 s at 380 °C leads to low hardness values in the center of the rod for Cu–Sb (Fig. 9b). An increase in annealing time to 3600 s results in inhomogeneous hardness profiles for Cu–Bi and Cu–Sb (Fig. 9c). For both materials, the lowest hardness values can now be found in the center of the rods. Annealing at temperatures of 920 °C leads to low, homogeneous cross-sectional hardnesses for all materials (Fig. 9d and e). The hardness of Cu–Bi is a little lower than the hardness of the other two materials (Fig. 9d and e). A comparison from Fig. 9d and e shows that increasing the annealing time from 900 to 3600 s does not lead to a further decrease in hardness.

3.2. Orientation imaging microscopy

In the following, inverse pole figure (IPF) maps are presented that show color-coded grain orientations in direction of the radial cross-section normals (Fig. 3). The IPF maps of all three materials in the as-swaged state *without* subsequent temperature exposure are shown in Fig. 10. After swaging, the deformed microstructure of the pure Cu rod in Fig. 10a differs from the microstructures of the alloyed materials (Fig. 10b and c). The grains in pure Cu are much finer, as has been discussed previously [27]. The Cu–Bi and Cu–Sb alloys exhibit no grain refinement even though they were exposed to the same processing sequence as pure Cu. The deformation textures of Cu–Bi and Cu–Sb consist almost exclusively of the two components ⟨1 1 1⟩ and ⟨0 0 1⟩, while pure Cu also shows other crystallographic orientations such as ⟨1 0 1⟩. Band-like features of strong localized deformation can be seen in the central region of Cu–Sb (Fig. 10c). These features seem to be confined to ⟨1 1 1⟩-oriented grains. Subsequent annealing at 380 °C for 900 s results in the fully recrystallized Cu microstructure shown in the IPF map of Fig. 11a. Grains of all crystallographic orientations are found. As already observed using optical microscopy, the same heat treatment does not trigger recrystallization in Cu–Bi (Fig. 6a and b). Here, recrystallization events are confined to regions of high localized deformation. In case of Cu–Sb, recrystallization has occurred in the central region of the rod. Recrystallized bands can be seen that bear close resemblance to the band-like deformation features shown in Fig. 10c.

Extending the duration of the heat treatment from 900 to 3600 s results in the partially recrystallized microstructures shown in Fig. 12. Most of the recrystallized grains are located close to the center of the rod for both Cu–Bi and Cu–Sb. The recrystallized volume fraction is significantly larger for Cu–Sb, where new grains have formed in the central part of the rod while the outer part appears to be less affected by recrystallization. In both alloys, grains which have *not* yet recrystallized often have ⟨0 0 1⟩ orientations (Fig. 12). ⟨1 1 1⟩-oriented grains appear to recrystallize more easily.

Kernel average misorientation (KAM) results are used to differentiate between recrystallized and non-recrystallized parts of the microstructure in Cu–Bi and Cu–Sb. Recently, this method was suc-

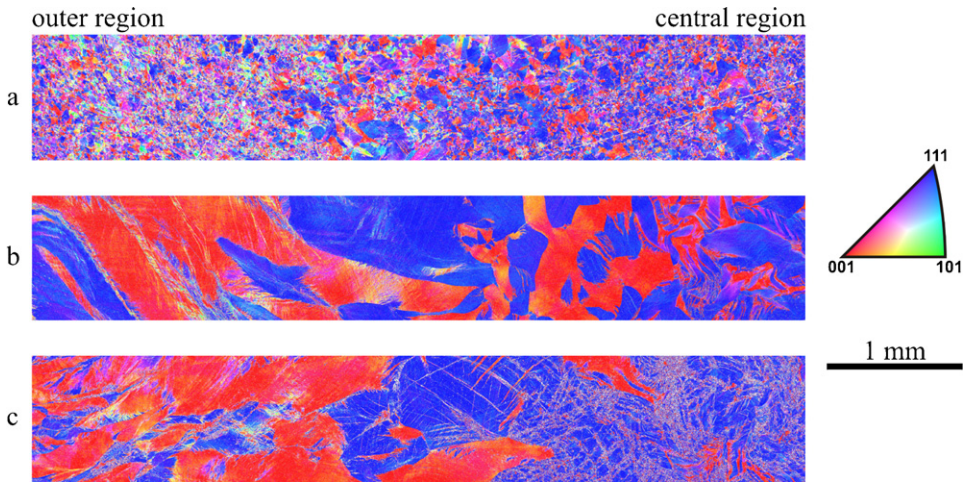

Fig. 10. Color-coded inverse pole figure (IPF) maps of the radial cross-sections of (a) Cu, (b) Cu–0.008 wt.% Bi, and (c) Cu–0.92 wt.% Sb rods after swaging.

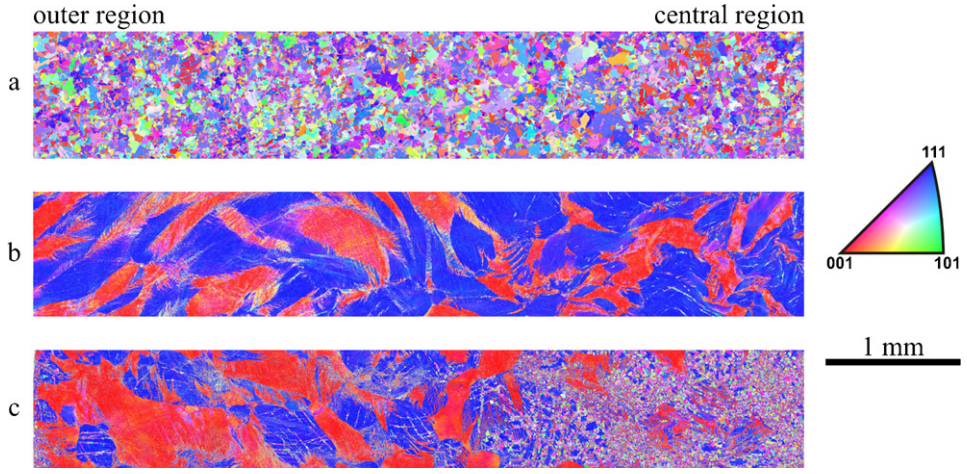

Fig. 11. Color-coded inverse pole figure (IPF) maps of the radial cross-sections of (a) Cu, (b) Cu–0.008 wt.% Bi, and (c) Cu–0.92 wt.% Sb rods after swaging and subsequent annealing at 380 °C for 900 s.

cessfully applied to the microstructure of an interstitial-free steel [31]. For each data point in the IPF maps of Fig. 12, the average misorientation with respect to the third nearest neighbors is calculated. A high degree of local plastic deformation is normally related to high local dislocation densities which give rise to high local misorientations [32]. Thus, recrystallized grains should exhibit low KAM values. A KAM threshold value of 2° is used to distinguish between recrystallized (KAM < 2°) and unrecrystallized (KAM > 2°) regions. The IPF maps in Fig. 13 contain only grains with a KAM value smaller than 2°. It is found in Fig. 13 that the majority of recrystallized grains exhibit orientations between ⟨1 0 1⟩ and ⟨1 1 1⟩. Grains with ⟨0 0 1⟩ orientations are rare.

Annealing at a temperature of 920 °C for 900 s results in the fully recrystallized microstructures shown in the IPF maps of Fig. 14 (corresponding grain size distributions were reported in Fig. 8). Fig. 14a indicates that Cu grains are large and often exhibit orientations close to ⟨0 0 1⟩ and ⟨1 1 1⟩. In contrast, the grains in Cu–Bi are smaller and mostly oriented close to ⟨1 0 1⟩ (Fig. 14b). Finally, the grains in Cu–Sb have the same size as in Cu–Bi, but their orientation appears to be more random and annealing twins are frequently observed.

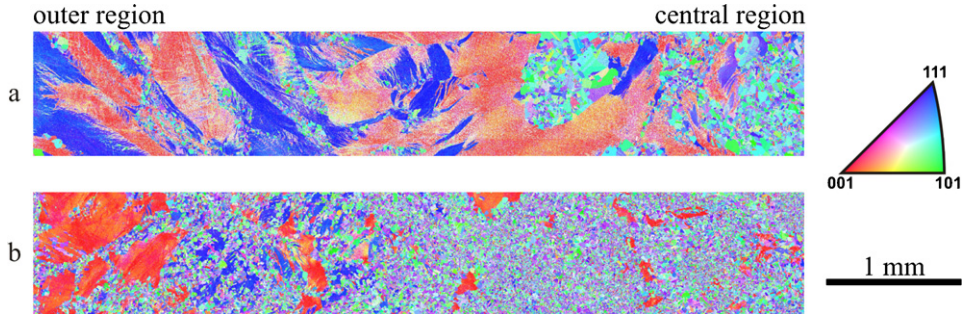

Fig. 12. Color-coded inverse pole figure (IPF) maps of the radial cross-sections of (a) Cu–0.008 wt.% Bi and (b) Cu–0.92 wt.% Sb rods after swaging and subsequent annealing at 380 °C for 3600 s.

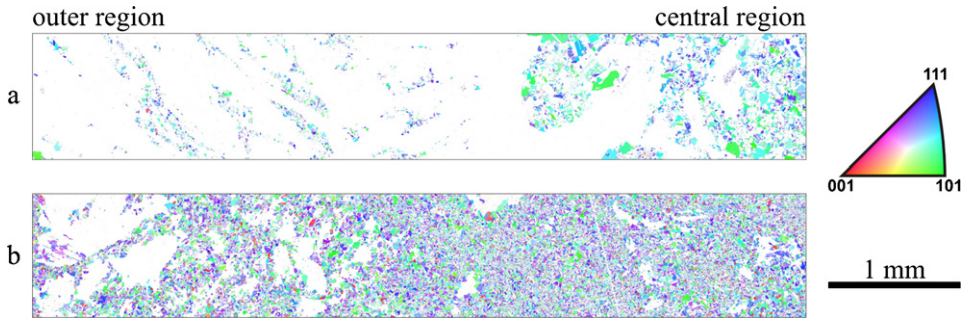

Fig. 13. Color-coded inverse pole figure (IPF) maps of Fig. 10 after removing grains with a KAM value greater than 2° (white areas).

Fig. 14 provides clear experimental evidence for an influence of small amounts of Bi and Sb on the evolution of texture in Cu.

4. Discussion

The addition of 0.008 wt.% Bi and 0.92 wt.% Sb to Cu affects the formation of microstructure during all steps of the processing chain beginning with the solidification process (left column of Fig. 4). Constitutional undercooling [33] accounts for the formation of dendrites in Cu–Sb which are absent in pure Cu [27] and Cu–Bi. Bi and Sb additions affect grain growth during solution annealing (right column of Fig. 4), which is a first indication for a segregation of these elements to grain boundaries where they slow down grain boundary mobility [34]. Moreover, Bi and Sb enforce work hardening during swaging. In agreement with results reported in the literature [35], where Sb was assessed to strongly promote work hardening in Cu, the highest hardness values are observed in Cu–Sb directly after swaging (Fig. 9a–c). Hardness profiles like those shown in Fig. 9, where the center exhibits higher hardness values than the outer regions, are typical for swaged rods [27,36–38]. They can be rationalized by cyclic softening in the outer regions [39]. The significant differences in hardness strongly decrease after a recrystallization treatment (Fig. 9d and e). This proves that the differences in hardness between the three alloys after swaging are not related to solid solution strengthening. Surprisingly, after recrystallization, the Cu–Bi alloy shows the lowest hardness values. The effect is small, but significant (Fig. 9d and e). This finding requires further investigation.

In the present work, we find evidence for strong localized deformation events during swaging of Cu–Sb, which were not observed to the same extent in Cu–Bi and pure Cu (Fig. 10c). This may be related to lower stacking fault energies [40], which result from the addition of Sb to Cu [41]. As expected from results of previous work [42,43], Bi and Sb additions have a strong effect on the kinetics of recrystallization by making it more difficult to trigger recrystallization. Higher temperatures are required to fully recrystallize Cu–Bi and Cu–Sb after swaging as compared to pure Cu. At temperatures where pure Cu fully recrystallizes, recrystallization in Cu–Bi and Cu–Sb remains incomplete.

As the most important result of our study, the recrystallization textures between Cu, Cu–Bi and Cu–Sb differ. While recrystallization of rotary swaged Cu bars results in the characteristic double fiber texture where ⟨1 1 1⟩ and ⟨0 0 1⟩ components dominate the grain structure [44], a strong ⟨1 0 1⟩ component governs the microstructure of Cu–Bi. Finally Cu–Sb, the third alloy considered here, seems to be less prone to the formation of a recrystallization texture and grain orientations are more random. The latter observation is in good agreement with results reported for recrystallization textures of drawn wires and cold-rolled sheets of Cu–Sb alloys [35,45,46]. Since the deformation textures of drawn wires and swaged rods are essentially the same [47], these results are thought to support the present experimental findings. It is suggested that the textural shift in Cu–Sb is again related to a reduction of stacking fault energy due to the addition of Sb. Twinning has been identified to be an important mechanism for the formation of new orientations during recrystallization in low SFE materials [48]. Furthermore, shear banding (Fig. 10c) is a more prominent deformation mechanism in low SFE materials [40], which can also produce highly misoriented recrystallization nuclei [49]. The textural shift observed in Cu–Bi (Fig. 14b) contradicts findings from the literature [45], where identical amounts of Bi resulted in no

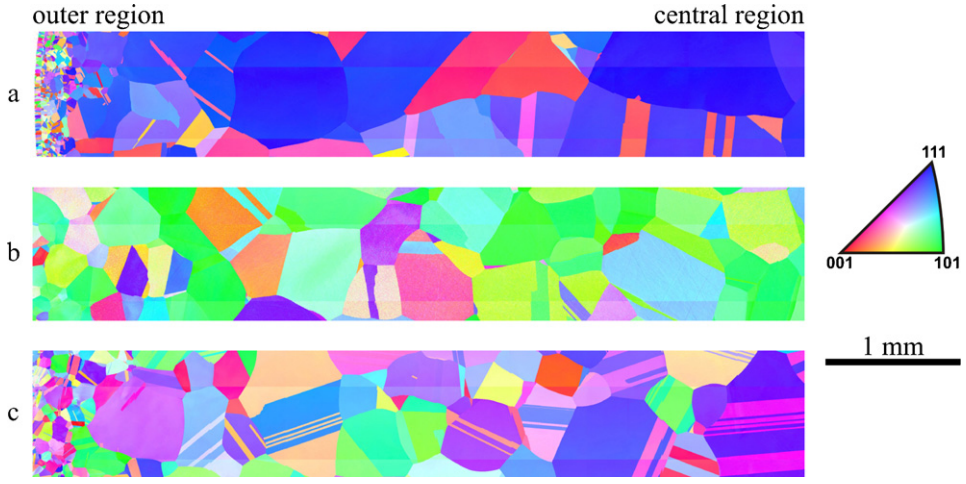

Fig. 14. Color-coded inverse pole figure (IPF) maps of the radial cross-sections of (a) Cu, (b) Cu–0.008 wt.% Bi, and (c) Cu–0.92 wt.% Sb rods after swaging and subsequent annealing at 920 °C for 900 s.

significant change in the recrystallization texture of drawn wires. The reason for the conflicting results remains unclear, however, since there is no evidence for a reduction of stacking fault energy in Cu–Bi, a grain growth controlled texture evolution cannot be ruled out. Inhomogeneous solute drag effects exerted by segregated Bi atoms, which strongly depend on the local grain boundary structure [34], could favor certain nuclei with a special misorientation relationship to grow faster than others. These nuclei then account for the recrystallization texture.

In summary, the present study shows that it is not possible to produce Cu, Cu–Bi and Cu–Sb microstructures which differ only in one respect, the presence or absence of Bi or Sb at grain boundaries. Low amounts of Bi and Sb in Cu affect solidification, work hardening and the evolution of microstructure and texture during thermomechanical treatments. This is important to remember when going further and discussing the effect of small amounts of Bi and Sb in Cu on the mechanical properties and on specific elementary damage processes like creep cavitation on grain boundaries.

5. Summary and conclusions

In the present study, the effect of small amounts of Bi and Sb additions on the evolution of microstructure in Cu was investigated. Previous microstructural and micromechanical results obtained from cylindrical Cu ingots (outer diameter of 40 mm), which were produced following an ingot metallurgy processing route (melting chunks of OFHC-Cu in a VIM furnace, casting and solidification, solution annealing, rotary swaging with intermediate and subsequent heat treatments), serve as reference data. New Cu–Bi and Cu–Sb ingots with 0.008 wt.% Bi or 0.92 wt.% Sb were produced following the same processing route, and the resulting microstructures were investigated. From the results obtained in the present study the following conclusions can be drawn:

(1) When small amounts of Bi and Sb are added to Cu, higher temperatures are needed to trigger recrystallization and to obtain homogeneous grain structures. Rotary swaged Cu fully recrystallizes at a temperature exposure of 380 °C for 900 s. Under the same conditions of temperature and annealing time Bi and Sb additions result in incomplete recrystallization of rotary swaged ingots.
(2) A heat treatment of the rotary swaged ingots of 900 s at 920 °C results in fully recrystallized microstructures in Cu, Cu–Bi and Cu–Sb. Evidence for preferential recrystallization in ⟨1 1 1⟩-oriented grains of the deformed microstructure was observed in Cu–Bi and Cu–Sb alloys.
(3) The cross-sectional hardness values in cylindrical rods obtained by rotary swaging differ between Cu, Cu–Bi, and Cu–Sb. The highest hardness values are observed for Cu–Sb, intermediate hardness values are observed for Cu–Bi, and the lowest for Cu. After recrystallization, the differences in hardness values are less pronounced. This represents indirect experimental evidence for Bi and Sb promoting work hardening in Cu.
(4) The addition of Bi and Sb to Cu affects the nature of the texture that is observed after swaging and subsequent recrystallization. While Cu shows the well-known double fiber texture (⟨1 1 1⟩ and ⟨0 0 1⟩ grain orientations parallel to longitudinal direction of the swaged rod), Bi-additions result in a strong ⟨1 0 1⟩ texture component. The addition of Sb also affects texture. Grains are more randomly distributed than in pure Cu.
(5) Sb additions to Cu appear to decrease the stacking fault energy. In the present study this manifests itself in two ways: first, Sb promotes localized deformation events (deformation bands in blue areas of Fig. 10c); second, Sb additions lead to the presence of a high density of straight annealing twins.

Acknowledgements

The authors acknowledge financial support by the Deutsche Forschungsgemeinschaft (DFG) through projects EG 101/13-1 and EG101/13–2. GE acknowledges support through his Max-Planck-Fellow research group at the Max-Planck Institut für Eisenforschung (MPIE), Düsseldorf. FO and JF acknowledge funding through the Advanced Study Group *Input Data and Validation* from the Interdisciplinary Centre for Advanced Materials Simulation (ICAMS) at the Ruhr University Bochum.

References

[1] T.B. Massalski (Ed.), Binary Alloy Phase Diagrams, ASM International, Materials Park, OH, 1990.
[2] L.-S. Chang, B.B. Straumal, E. Rabkin, W. Gust, F. Sommer, J. Phase Equilib. 18 (1997) 128–135.
[3] W. Hampe, Z. Berg- Huetten- Salinenwes. Preuss. Staate 23 (1874) 93–137.
[4] D. McLean, L. Northcott, J. Inst. Met. 72 (1946) 583–616.
[5] E. Voce, A.P.C. Hallowes, J. Inst. Met. 73 (1947) 323–376.
[6] D. McLean, J. Inst. Met. 81 (1952) 121–123.
[7] A. Joshi, D.F. Stein, J. Inst. Met. 99 (1971) 178–181.
[8] B.D. Powell, H. Mykura, Acta Metall. 21 (1973) 1151–1156.
[9] S.F. Baumann, D.B. Williams, J. Microsc. 123 (1981) 299–305.
[10] T.H. Chuang, W. Gust, L.A. Heldt, M.B. Hintz, S. Hofmann, R. Lucic, B. Predel, Scr. Metall. 16 (1982) 1437–1441.
[11] J.R. Michael, D.B. Williams, Metall. Trans. A 15A (1984) 99–105.
[12] A.M. Donald, L.M. Brown, Acta Metall. 27 (1979) 59–66.
[13] J.C. Earthman, J.C. Gibeling, W.D. Nix, Acta Metall. 33 (1985) 805–817.
[14] G.H. Li, L.D. Zhang, Scr. Metall. Mater. 32 (1995) 1335–1340.
[15] D.E. Luzzi, M. Yan, M. Šob, V. Vitek, Phys. Rev. Lett. 67 (1991) 1894–1897.
[16] V.J. Keast, J. Bruley, P. Rez, J.M. Maclaren, D.B. Williams, Acta Mater. 46 (1998) 481–490.
[17] U. Alber, H. Müllejans, M. Rühle, Acta Mater. 47 (1999) 4047–4060.
[18] L.-S. Chang, E. Rabkin, B.B. Straumal, B. Baretzky, W. Gust, Acta Mater. 47 (1999) 4041–4046.
[19] R. Monzen, O. Matsuda, H. Miura, Z. Metallkd. 93 (2002) 840–844.
[20] V.J. Keast, A. La Fontaine, J. du Plessis, Acta Mater. 55 (2007) 5149–5155.
[21] R.K. Rajgarhia, D.E. Spearot, A. Saxena, Modell. Simul. Mater. Sci. Eng. 17 (2009) 1–13.
[22] E.D. Hondros, D. McLean, Philos. Mag. 29 (1974) 771–795.
[23] G. Duscher, M.F. Chisholm, U. Alber, M. Rühle, Nat. Mater. 3 (2004) 621–626.
[24] S. Lassmann, W. Reif, Metall 51 (1997) 186–189.
[25] M. Sadayappan, J.P. Thomson, M. Sahoo, H.T. Michels, in: J.-M. Welter (Ed.), Copper, Proc. of the Int. Conf. Copper'06, Wiley-VCH, Weinheim, 2006, pp. 179–184.
[26] P.C. Millett, R.P. Selvam, A. Saxena, Acta Mater. 55 (2007) 2329–2336.
[27] F. Otto, J. Frenzel, G. Eggeler, Int. J. Mater. Res., accepted for publication.
[28] L.-S. Chang, E. Rabkin, S. Hofmann, W. Gust, Acta Mater. 47 (1999) 2951–2959.
[29] K.S. Yu, A. Joshi, W.D. Nix, Metall. Trans. A 14A (1983) 2447–2454.
[30] E. Weck, E. Leistner, Metallographic Instructions for Colour Etching by Immersion Part I: Klemm Colour Etching, DVS, Düsseldorf, 1982.
[31] S. Dziaszyk, E.J. Payton, F. Friedel, V. Marx, G. Eggeler, Mater. Sci. Eng. A 527 (2010) 7854–7864.
[32] A.J. Schwartz, M. Kumar, B.L. Adams (Eds.), Electron Backscatter Diffraction in Materials Science, Kluwer Academic, New York, NY, 2000.
[33] D.M. Stefanescu, Science and Engineering of Casting Solidification, Kluwer Academic/Plenum Publishers, New York, 2002.
[34] A.P. Sutton, R.W. Balluffi, Interfaces in Crystalline Materials, Clarendon Press, Oxford, 1996.
[35] R.M. Brick, D.L. Martin, R.P. Angier, Trans. Am. Soc. Met. 31 (1943) 675–698.
[36] A. Grabianowski, B. Danda, B. Ortner, H.P. Stüwe, Mech. Res. Commun. 7 (1980) 125–126.
[37] B. Ortner, A. Grabianowski, A. Danda, Aluminium 58 (1982) 657–659.
[38] M.F. Hupalo, A.F. Padilha, H.R.Z. Sandim, A.M. Kliauga, ISIJ Int. 44 (2004) 1894–1901.
[39] J. Schrank, H.P. Stüwe, Z. Metallkd. 77 (1986) 107–111.
[40] R.E. Smallman, R.J. Bishop, Modern Physical Metallurgy and Materials Engineering, sixth ed., Elsevier, Oxford, 1999.
[41] L. Deléhouzée, A. Deruyttere, Acta Metall. 15 (1967) 727–734.
[42] F. Haessner, G. Hoschek, G. Tölg, Acta Metall. 27 (1979) 1539–1548.
[43] A. Lucci, Scr. Metall. 11 (1981) 1127–1130.
[44] R.O. Williams, Acta Metall. 13 (1965) 163–168.
[45] P.G. Bastien, J. Pokorny, J. Inst. Met. 82 (1953/1954) 545–549.
[46] R.H. Richman, Y.C. Liu, Trans. Metall. Soc. AIME 221 (1961) 720–732.
[47] C.S. Barrett, T.B. Massalski, Structure of Metals, third ed., McGraw-Hill, New York, 1966.
[48] A. Berger, P.-J. Wilbrandt, F. Ernst, U. Klement, P. Haasen, Prog. Mater. Sci. 32 (1988) 1–95.
[49] H. Paul, J.H. Driver, C. Maurice, Z. Jasienski, Acta Mater. 50 (2002) 4339–4355.